

Entropy-based viscous regularization for the multi-dimensional Euler equations in low-Mach regimes

Marc O. Delchini^a, Jean C. Ragusa^{*,a}, Ray A. Berry^b

^a*Department of Nuclear Engineering, Texas A&M University, College Station, TX 77843, USA*

^b*Idaho National Laboratory, Idaho Falls, ID 83415, USA*

Abstract

The entropy viscosity method, introduced by Guermond et al. [1, 2], is extended to the multi-dimensional Euler equations for both subsonic (very low Mach numbers) and supersonic flows. We show that the current definition of the viscosity coefficients [1] is not adapted to low-Mach flows and we provide a robust alternate definition valid for any Mach number value. The new definitions are derived from a low-Mach asymptotic study. In addition, the entropy minimum principle is used to derive the viscous regularization terms for Euler equations with variable area for nozzle flow problems. Various 1- and 2-D numerical tests are presented : flow in a convergent-divergent nozzle, Leblanc shock tube, subsonic flow around a 2-D cylinder and over a circular hump, and supersonic flow in a compression corner. Convergence studies are performed using analytical solutions in 1-D. Both the ideal gas and stiffened gas equations of state are employed.

Key words: Euler equations with variable area, entropy viscosity method, stabilization method, low Mach regime, shocks.

1. Introduction

I think we should focus the introduction more

Incompressible flows are a particular case of compressible ones and therefore in principle, a compressible flow solver should be able to compute these flows. Unfortunately, there are experimental evidences showing that on a fixed mesh, the solutions of the compressible flow discretized equations are not an accurate approximation of the solutions of the incompressible model (e.g. see [29]). A first analysis of this problem appeared in [23] and this question has drawn a considerable attention [13,7,9,26,28,30] in the recent past. Several works have tried to explain the reasons of this difficulty and to construct numerical schemes valid

*Corresponding author

Email addresses: `delchmo@tamu.edu` (Marc O. Delchini), `jean.ragusa@tamu.edu` (Jean C. Ragusa), `ray.berry@inl.gov` (Ray A. Berry)

for all Mach numbers. Some of these works extend to the compressible regime the numerical methods used for the computation of incompressible flows. Examples of these type of methods are for instance [1] or [30]. Another approaches rely on some modifications of high order shock capturing techniques. These approaches are for instance described in [2,7,22] for Roe discretization, in [3] for the HLLE scheme and in [28] for Flux schemes. Their principal ingredient is the use of preconditioning techniques originally developed for steady state computations [4,21,23] that are here selectively applied only to the upwind artificial viscosity.

The efficient simulation of low Mach number flows is a subject of ongoing discussion in the CFD community. While the flow is expected to be incompressible, in a lot of applications the Mach number or the compressibility properties vary strongly in time or space. This is for example the case in nozzle flow, chemically reacting flows or laminar combustion. It is well known that purely compressible flow solvers which were developed for transonic flow produce wrong results at low Mach numbers. On the other hand, standard incompressible flow solvers cannot deal with strong temperature or strong density gradients. This sets a demand for codes that can deal with flows at all Mach numbers.

It is well known that it is difficult to solve the compressible equations for low Mach numbers. For an explicit scheme this is easily seen by looking at the time steps. For stability the time step must be chosen inversely proportional to the largest eigenvalue of the system which is approximately the speed of sound, c , for slow flows. However, other waves are convected at the fluid speed, u , which is much slower. Hence, these waves don't change very much over a time step. Thus, thousands of time steps are required to reach a steady state. Should one try a multigrid acceleration one finds that the same disparity in wave speeds slows down the multigrid acceleration. With an implicit method an AD1 factorization is usually used so that one can easily invert the implicit factors. The use of AD1 introduces factorization errors which again slow down the convergence rate when there are wave speeds of very different magnitudes. For small Mach numbers it can be shown [28,31] that the incompressible equations approximate the compressible equations. Hence, one needs to justify the use of the compressible equations for low Mach flows. We present several reasons why one would still use the compressible equations even though the Mach number of the flow is small. There are many sophisticated compressible codes available that could be used for such problems especially in complicated geometries. For low speed aerodynamic problems at a high angle of attack most of the flow consists of a low Mach number flow. However, there are localized regions containing shocks. In many problems thermal effects are important and the energy equation is coupled to the other equations.

The incompressible limit of a compressible flow is rather subtle due to the fact that the propagation rate of the pressure waves becomes infinite and the equations change their type. Within this limit the pressure splits up into a thermodynamic pressure term and a hydrodynamic pressure term. If the limit solution has constant temperature and density and if the boundary values satisfy the incompressibility constraint, then the thermodynamic pressure becomes

57 the background pressure being constant in space and time. The hydrodynamic
 58 pressure appears in the incompressible equations as a sort of a Lagrangian mul-
 59 tiplier with no connection to the equation of state. The asymptotic analysis
 60 of Klainerman and Majda in [9,10] gives insight into this limit behavior. They
 61 gave a mathematically rigorous derivation in the isentropic case. The asymp-
 62 totic analysis was formally extended by Klein to the non-isentropic case and
 63 to multiple space scales in [11] in which he also gave an overview about other
 64 asymptotic considerations in this low Mach number regime. A detailed dis-
 65 cussion of the incompressible limit is also given in the book of Wesseling [20].
 66 Numerical methods for the compressible equations may have difficulties with the
 67 zero Mach number limit because in the limit the speed of sound waves becomes
 68 infinite compared to the flow speed and thus leads to an elliptic coupling of pres-
 69 sure and velocity. Hence, all explicit numerical schemes become quite inefficient
 70 in the low Mach number regime due to their stability restriction (CFL condi-
 71 tion). The other difficulty is that the pressure in the compressible equations
 72 converges to the thermodynamic pressure, which becomes the constant back-
 73 ground pressure in the incompressible limit. This is the way how the equation
 74 of state for compressible flow is automatically satisfied and does not appear in
 75 the incompressible equations. For the compressible equations Bijl and Wesseling
 76 [2] introduced a splitting of the pressure into a thermodynamic and a hydrody-
 77 namic pressure term. Then they proposed an implicit numerical method that
 78 remains stable without reference to the sound velocity and which approximates
 79 the incompressible equations for Mach number zero. The constant thermody-
 80 namic pressure satisfies the equation of state and the hydrodynamic pressure
 81 serves as a Lagrangian multiplier to get the divergence-free property of the ve-
 82 locity. A formulation in conservative variables was later given in [18,20]. Similar
 83 to this approach Klein and Munz [12] and Munz et al. [13] proposed the multi-
 84 ple pressure variable (MPV) method based on the asymptotic results of Klein
 85 [11].

86 above are good snippets from some papers.

87 Over the past years an increasing interest raised for computational meth-
 88 ods that can solve both compressible and incompressible flows. In engineering
 89 applications, there is often the need to solve for complex flows where a near
 90 incompressible regime or low Mach flow coexists with a supersonic flow domain.
 91 For example, such flow are encountered in aerodynamic in the study of airships.
 92 In the nuclear industry, flows are nearly the incompressible regime but com-
 93 pressible effects cannot be neglected because of the heat source and thus needs
 94 to be accurately resolved.

95 When solving the multi-D Euler equations for a wide range of Mach numbers,
 96 multiple problems have to address: stability, accuracy and acceleration of the
 97 convergence in the low Mach regime. Because of the hyperbolic nature of the
 98 equations, shocks can form during transonic and supersonic flows, and require
 99 the use of the numerical methods in order to stabilize the scheme and cor-
 100 rectly resolve the discontinuities. The literature offers a wide range of stabiliza-
 101 tion methods: flux-limiter [3, 4], pressure-based viscosity method ([5]), Lapidus
 102 method ([6, 7, 8]), and the entropy-viscosity method([1, 2]) among others. These

numerical methods are usually developed using simple equation of states and tested for transonic and supersonic flows where the disparity between the acoustic waves and the fluid speed is not large since the Mach number is of order one. This approach leads to a well-known accuracy problem in the low Mach regime where the fluid velocity is smaller than the speed of sound by multiple order of magnitude. The numerical dissipative terms become ill-scaled in the low Mach regime and lead to the wrong numerical solution by changing the nature of the equations solved. This behavior is well documented in the literature [9, 10, 11] and often treated by performing a low Mach asymptotic study of the multi-D Euler equation. This method was originally used [9] to show convergence of the compressible multi-D Euler equations to the incompressible ones. Thus, by using the same method, the effect of the dissipative terms in the low Mach regime, can be understood and, when needed, a fix is developed in order to ensure the convergence of the equations to the correct physical solution. This approach was used as a fixing method for multiple well known stabilization methods alike Roe scheme ([12]) and SUPG [11] while preserving the original stabilization properties of shocks.

We propose, through this paper, to investigate how the entropy viscosity method, when applied to the multi-D Euler equations with variable area, behaves in the low Mach regime. This method was initially introduced by Guermond et al. to solve for the hyperbolic systems and has shown good results when used for solving the multi-D Euler equations with various discretization schemes. More importantly, it is simple to implement, can be used with unstructured grids, and its dissipative terms are consistent with the entropy minimum principle and proven valid for any equation of state under certain conditions [13].

This paper is organized as follows: in Section 2 the current definition of the entropy viscosity method is recalled, and inconsistency with the low Mach regime are pointed out. Since our interest is in the variable area version of the multi-D Euler equation, the reader is guided through the steps leading to the derivation of the dissipative terms on the model of [13]. Then in Section 3, a new definition of the viscosity coefficient is introduced and derived from a low Mach asymptotic study. After detailing the spatial and temporal discretization method in Section 4, 1- and 2-D numerical results are presented in Section 5 for a wide range of Mach numbers: low Mach flow over a cylinder and a circular bump, and supersonic flow in a compression corner [14]. Convergence studies are performed in 1-D, in order to demonstrate the accuracy of the solution.

I wouldn't recall this here. Let me think about that.

For purpose of clarity, the multi-D Euler equations with variable area are recalled in Eq. (1) and the corresponding variables are defined:

$$\begin{cases} \partial_t (\rho A) + \vec{\nabla} \cdot (\rho \vec{u} A) = 0 \\ \partial_t (\rho \vec{u} A) + \vec{\nabla} \cdot [(\rho \vec{u} \otimes \vec{u} + P \mathbf{I}) A] = P \vec{\nabla} A \\ \partial_t (\rho E A) + \vec{\nabla} \cdot [\vec{u} (\rho E + P) A] = 0 \\ P = P(\rho, e) \end{cases} \quad (1)$$

where ρ , $\rho \vec{u}$ and ρE are the density, the momentum and the total energy, re-

spectively, and will be referred to as the conservative variables. The pressure P is computed with an equation of state expressed in function of the density ρ and the specific internal energy e . The tensor product $\vec{a} \otimes \vec{b}$ is taken with the following convention: $(\vec{a} \otimes \vec{b})_{i,j} = a_i b_j$. Lastly, the terms ∂_t , $\vec{\nabla}$, $\vec{\nabla} \cdot$ and \mathbf{I} denote the temporal derivative, the gradient and divergent operators, and the identity tensor, respectively. The variable area A is assumed spatial dependent.

2. The Entropy Viscosity Method

2.1. Background

In this section, the entropy-based viscosity method [1, 2, 15] is recalled for the multi-D Euler equations (with constant area A) [16]. The entropy-based viscosity method consists of adding dissipative terms, with a viscosity coefficient modulated by the entropy production which allows high-order accuracy when the solution is smooth. Thus, two questions arise: (i) how are the viscosity dissipative terms derived and (ii) how to numerically compute the entropy production. Answers to the first question can be found in [13] by Guermond et al., that details the proof leading to the derivation of the artificial dissipative terms (Eq. (2)) consistent with the entropy minimum principle theorem. The viscous regularization obtained is valid for any equation of state as long as the opposite of the physical entropy function, s , is convex with respect to the internal energy e and the specific volume $1/\rho$. As for the entropy production, it is locally evaluated by computing the local entropy residual $D_e(\vec{x}, t)$ defined in Eq. (4), that is known to be peaked in shocks [17].

$$\begin{cases} \partial_t(\rho) + \vec{\nabla} \cdot (\rho \vec{u}) = \vec{\nabla} \cdot (\kappa \vec{\nabla} \rho) \\ \partial_t(\rho \vec{u}) + \vec{\nabla} \cdot (\rho \vec{u} \otimes \vec{u} + P \mathbf{I}) = \vec{\nabla} \cdot (\mu \rho \vec{\nabla}^s \vec{u} + \kappa \vec{u} \otimes \vec{\nabla} \rho) \\ \partial_t(\rho E) + \vec{\nabla} \cdot [\vec{u}(\rho E + P)] = \vec{\nabla} \cdot (\kappa \vec{\nabla}(\rho e) + \frac{1}{2} \|\vec{u}\|^2 \kappa \vec{\nabla} \rho + \rho \mu \vec{u} \vec{\nabla} \vec{u}) \\ P = P(\rho, e) \end{cases} \quad (2)$$

where κ and μ are local positive viscosity coefficients. $\vec{\nabla}^s \vec{u}$ denotes the symmetric gradient operator that guarantees the method to be rotational invariant [13].

In the current version of the method, κ and μ are set equal, so that the above viscous regularization (Eq. (2)) is equivalent to the parabolic regularization [18] when considering the 1-D form of the equation. The current definition includes a first-order viscosity coefficient referred to with the subscript max , and a high-order viscosity coefficient referred to with the subscript e . The first-order viscosity coefficients μ_{max} and κ_{max} are proportional to the local largest eigenvalue $\|\vec{u}\| + c$ and equivalent to an upwind-scheme (see Eq. (3)), when used, which is known to be over-dissipative and monotone [17]:

$$\mu_{max}(\vec{r}, t) = \kappa_{max}(\vec{r}, t) = \frac{h}{2} (\|\vec{u}\| + c), \quad (3)$$

176 where h is defined as the ratio of the grid size to the polynomial order of the
177 test functions used.

178 The second-order viscosity coefficients κ_e and μ_e are set proportional to the
179 entropy production that is evaluated by computing the local entropy residual
180 D_e . It also includes the interfacial jump of the entropy flux J that will allow to
181 detect any discontinuities other than shocks:

$$\mu_e(\vec{r}, t) = \kappa_e(\vec{r}, t) = h^2 \frac{\max(|D_e(\vec{r}, t)|, J)}{\|s - \bar{s}\|_\infty} \text{ with } D_e(\vec{r}, t) = \partial_t s + \vec{u} \cdot \vec{\nabla} s \quad (4)$$

182 where $\|\cdot\|_\infty$ and $\bar{\cdot}$ denote the infinite norm operator and the average operator
183 over the entire computational domain, respectively. The definition of the jump
184 J is discretization-dependent and examples of definition can be found in [16]
185 for DGFEM. The denominator $\|s - \bar{s}\|_\infty$ is used for dimensionality purposes
186 and should not be of the same order as h , on penalty of loosing the high-
187 order accuracy. Currently, there are no theoretical justification for choosing the
188 denominator.

189 The definition of the viscosity coefficients μ and κ is function of the first- and
190 second-order viscosity coefficients as follows:

$$\mu(\vec{r}, t) = \min(\mu_e(\vec{r}, t), \mu_{max}(\vec{r}, t)) \text{ and } \kappa(\vec{r}, t) = \min(\kappa_e(\vec{r}, t), \kappa_{max}(\vec{r}, t)). \quad (5)$$

191 This definition allows the following properties. In shock regions, the second-
192 order viscosity coefficient experiences a peak because of entropy production, and
193 thus, saturates to the first-order viscosity that is known to be over-dissipative
194 and will smooth out oscillations. Anywhere else, the entropy production being
195 small, the viscosity coefficients μ and κ are of order h^2 .

196 Using the above definition of the entropy-based viscosity method, high-order
197 accuracy was demonstrated and excellent results were obtained with 1-D Sod
198 shock tubes and various 2-D tests [1, 2, 16].

199 2.2. Issues in the Low-Mach Regime

200 In the Low-Mach Regime, the flow is known to be isentropic resulting in
201 very little entropy production. Since the entropy viscosity method is directly
202 based on the evaluation of the local entropy production, it will be interested
203 to study how the entropy viscosity coefficients μ and κ scale in the low Mach
204 regime. Mathematically, it means that the entropy residual D_e will be very
205 small, so will be the denominator $\|s - \bar{s}\|_\infty$, thus making the ratio, used in
206 the definition of the viscosity coefficients Eq. (4), undetermined. Therefore, the
207 current definition of the viscosity coefficients seems unadapted to subsonic flow
208 and could lead to ill-scaled dissipative terms. A solution would be to recast
209 the entropy residual as a function of other variables in order to have more
210 freedom in the choice of the normalization parameter. With this approach, the
211 viscosity coefficients are still defined proportional to the entropy residual that
212 is a good indicator of the flow type (subsonic, transonic and supersonic flow).
213 Plus, a different normalization parameter could be chosen, based on a low Mach
214 asymptotic study so that the viscosity coefficients are well-scaled in the low
215 Mach asymptotic limit (see Section 3).

216 *2.3. The dissipative-terms for the multi-D Euler equations with variable area*

217 One of the focus of this paper is to investigate the application of the entropy
 218 viscosity method to the multi-D Euler equations with variable area. The variable
 219 area version of the Euler equations is mostly used in 1-D and 2-D for obvious
 220 reasons, and differs from Eq. (1) by the momentum equation as shown in Eq. (6),
 221 that contains a non-conservative term proportional to the area gradient. For
 222 the purpose of this paper, the variable area is assumed to be a smooth function
 223 and only spatial dependent. An example can be found in [19] where a fluid flows
 224 through a 1-D convergent-divergent nozzle and reaches a steady-state solution.

$$\begin{cases} \partial_t (\rho A) + \vec{\nabla} \cdot (\rho \vec{u} A) = 0 \\ \partial_t (\rho \vec{u} A) + \vec{\nabla} \cdot [A (\rho \vec{u} \otimes \vec{u} + P \mathbf{I})] = P \vec{\nabla} A \\ \partial_t (\rho E) + \vec{\nabla} \cdot [\vec{u} (\rho E + P)] = 0 \end{cases} \quad (6)$$

225 The application of the entropy viscosity method to the above system of equa-
 226 tions is expected to be straightforward since it degenerates to the Eq. (1) when
 227 assuming a constant area. Details of the derivations of the dissipative terms are
 228 available to the reader in Appendix B and are very similar to what was done
 229 in [13]. An entropy residual is derived without the dissipative terms. Then,
 230 the same entropy residual is re-derived after adding dissipative terms to each
 231 equation of the system given in Eq. (6), and the entropy minimum principle is
 232 used as a condition to obtain a definition for each of the dissipative terms. The
 233 final result including the dissipative terms is given in Eq. (7):

$$\begin{cases} \partial_t (\rho A) + \vec{\nabla} \cdot (\rho \vec{u} A) = \vec{\nabla} \cdot (A \kappa \vec{\nabla} \rho) \\ \partial_t (\rho \vec{u} A) + \vec{\nabla} \cdot [A (\rho \vec{u} \otimes \vec{u} + P \mathbf{I})] = P \vec{\nabla} A + \vec{\nabla} \cdot \left[A \left(\mu \rho \vec{\nabla}^s \vec{u} + \kappa \vec{u} \otimes \vec{\nabla} \rho \right) \right] \\ \partial_t (\rho E) + \vec{\nabla} \cdot [\vec{u} (\rho E + P)] = \vec{\nabla} \cdot \left[A \left(\kappa \vec{\nabla} (\rho e) + \frac{1}{2} \|\vec{u}\|^2 \kappa \vec{\nabla} \rho + \rho \mu \vec{u} \vec{\nabla} \vec{u} \right) \right] \end{cases} \quad (7)$$

234 The dissipative terms are very similar to the ones obtained for the multi-D Euler
 235 equations: each dissipative flux is multiplied by the variable area A in order to
 236 ensure conservation of the flux. When assuming a constant area, Eq. (2) is
 237 retrieved. The definition of the viscosity coefficients μ and κ is explained in
 238 Section 3.2.

239 **3. All-speed Reformulation of the Entropy Viscosity Method**

240 In this section, the entropy residual D_e is recast as a function of the pressure,
 241 the density and the speed of sound. Then, a low Mach asymptotic study of the
 242 multi-D Euler equations is performed in order to derive the correct normalization
 243 parameter.

244 *3.1. New Entropy Production Residual*

245 The first step in defining a viscosity coefficient that behaves well in the low
 246 mach limit is to recast the entropy residual in terms of the thermodynamic

variables as shown in Eq. (8):

$$D_e(\vec{r}, t) = \partial_t s + \vec{u} \cdot \vec{\nabla} s = \frac{s_e}{P_e} \left(\underbrace{\frac{dP}{dt} - c^2 \frac{d\rho}{dt}}_{\tilde{D}_e(\vec{r}, t)} \right), \quad (8)$$

where $\frac{d}{dt}$ denotes the material or total derivative, and P_e is the partial derivative of pressure with respect to internal energy. The steps that lead to the new formulation of the entropy residual D_e can be found in Appendix A.

The entropy residual D_e and \tilde{D}_e are proportional to each other and therefore will experience the same variation when taking the absolute value. Thus, locally evaluating \tilde{D}_e instead of D_e should allow us to measure the entropy production point wise. This new expression given in Eq. (8) has multiple advantages:

- an analytical expression of the entropy function is not longer needed: the entropy residual \tilde{D}_e is evaluated using the local values of the pressure, the density and the speed of sound. Deriving an entropy function for some complex equation of states can be difficult.
- with the proposed expression of the entropy residual function of pressure and density, additional normalizations suitable for low Mach flows of the entropy residual can be devised. Examples include the pressure itself, or combination of the density, the speed of sound and the norm of the velocity: ρc^2 , $\rho c ||\vec{u}||$ and $\rho ||\vec{u}||^2$.

The viscosity coefficients μ and κ are now defined proportional to the new entropy residual \tilde{D}_e on the model of Eq. (4) as follows:

$$\mu(\vec{r}, t) = \kappa(\vec{r}, t) = h^2 \frac{\max(\tilde{D}_e, J)}{n(P)} \quad (9)$$

where $n(P)$ is a normalization parameter to determine and all other variables were defined previously.

As mentioned earlier, the normalization parameter $n(P)$ must be of the same units as the pressure for the viscosity coefficients to have the unit of a dynamic viscosity (m^2/s). Multiples options are available to us: P , ρc^2 , $\rho c ||\vec{u}||$ and $\rho ||\vec{u}||^2$. The choice of the normalization parameter cannot be random if the definition of the viscosity coefficient is wanted to be well-scaled for a wide range of Mach numbers. For example, by choosing $n(P) = \rho ||\vec{u}||^2$, the viscosity coefficient will become very large as the Mach number decreases which would be unnecessary since the equations will not develop any shock or discontinuity. Therefore, it is proposed to carry, in Section 3.2, a low-Mach asymptotic study of the multi-D Euler equations in order to determine the correct expression for the normalization parameter $n(P)$.

3.2. Low-Mach asymptotic study of the multi-D Euler equations

The asymptotic study requires the multi-D Euler equations to be non dimensionalized: the objective is to make the Mach number appears and thus, use a polynomial expansion of the variables as a function of the Mach number in order to derive the leading, first- and second-order equations. Before detailing the steps of the asymptotic method, let us have a closer look at the system of equations under consideration. The initial system of equations is composed of the multi-D Euler equations. For stability purpose, artificial dissipative terms are added to each equation as explained in Section 2. The resulting system of equations is alike the multi-D Navier-Stokes equations in a sense that it contains second-order derivative terms. Thus, it would be interesting to look at the steps employed in the asymptotic study of the multi-D Navier-Stokes equations in order to understand how the dissipative terms are treated. Fortunately, this process is well-documented in the literature [9, 10, 11] for both multi-D Euler equations and Navier-Stokes equations. The work presented here is mainly inspired of [20] that focuses on the asymptotic study in the low Mach regime of Navier-Stokes equations. During the derivation, the reader has to keep in mind that the objective of this section is to derive the scaling of the normalization parameter $n(P)$ involved in the definition of the viscosity coefficients given in Eq. (4), so that the multi-D Euler equations degenerate to the incompressible system of equations, which implies that the dissipative terms are well-scaled. The main steps of the derivation are presented in the following of this section. To express Eq. (2) in dimensionless variables, the following dimensional variables are introduced:

$$\begin{aligned}\rho &= \frac{\rho^*}{\rho_\infty}, P = \frac{P^*}{\rho_\infty c_\infty^2}, \mu = \frac{\mu^*}{\mu_\infty}, E = \frac{E^*}{c_\infty^2}, \mu = \frac{\mu^*}{\mu_\infty}, \\ \kappa &= \frac{\kappa^*}{\kappa_\infty}, x = \frac{x^*}{L_\infty}, t = \frac{t^*}{L_\infty/u_\infty}, u = \frac{u^*}{u_\infty}\end{aligned}\quad (10)$$

where the subscript ∞ and the upper script $*$ denote the far field or stagnation quantities and the dimensionless variables, respectively. The reference quantities are chosen such that the non dimensional flow quantities are of order one for any low reference-Mach number

$$M_\infty = \frac{u_\infty^*}{c_\infty^*} \quad (11)$$

where c_∞^* is a reference value for the speed of sound.

Then, using the non dimensional quantities and the multi-D Euler equations from Eq. (2), the following non dimensional form is obtained:

$$\begin{cases} \partial_t \rho + \nabla \cdot (\rho \vec{u}) = \frac{1}{Re_\infty Pr_\infty} \nabla \cdot (\kappa \nabla \rho) \\ \partial_t (\rho \vec{u}) + \nabla \cdot (\rho \vec{u} \otimes \vec{u}) + \frac{1}{M_\infty^2} \nabla (P) = \frac{1}{Re_\infty} \nabla \cdot (\rho \mu \nabla \vec{u}) + \frac{1}{Re_\infty^2 Pr_\infty} \nabla \cdot (\vec{u} \otimes \kappa \nabla \rho) \\ \partial_t (\rho E) + \nabla \cdot [\vec{u} (\rho E + P)] = \frac{1}{Re_\infty Pr_\infty} \nabla \cdot (\kappa \nabla (\rho e)) + \frac{\tilde{M}_\infty^2}{Re_\infty} \nabla \cdot (\vec{u} \rho \mu \nabla \vec{u}) \\ + \frac{M_\infty^2}{2 Re_\infty Pr_\infty} \nabla \cdot (\kappa u^2 \nabla \rho) \\ P = (\gamma - 1) (\rho E + M_\infty^2 \rho u^2) \end{cases} \quad (12)$$

where the *numerical* Reynolds (Re_∞) and Prandtl (Pr_∞) numbers are defined as follows:

$$Re_\infty = \frac{u_\infty L_\infty}{\mu_\infty} \text{ and } Pr_\infty = \frac{\mu_\infty}{\kappa_\infty}. \quad (13)$$

Once the dimensionless equations are obtained, the next step consists of expanding each variable in term of the Mach number (example given in Eq. (14) for the pressure P) in order to derive the leading, first- and second-order equations.

$$P(\vec{r}, t) = P_0(\vec{r}, t) + P_1(\vec{r}, t)M_\infty + P_2(\vec{r}, t)M_\infty^2 + \dots \text{ with } M_\infty \rightarrow 0 \quad (14)$$

From Eq. (15), it is observed that the scaling of the Reynolds and Prandtl numbers will affect the asymptotic equations because of the dissipative terms. By studying the effect of the dissipative terms onto the asymptotic equations, the scaling of the viscosity coefficients μ and κ can be determined so that the pressure and velocity fluctuations remain of the order of the Mach number square and the Mach number, respectively. For the purpose of this section it is assumed that the Reynolds and Prandtl numbers scale as the Mach number to the power n and m , respectively: $Re_\infty = M_\infty^n$ and $Pr_\infty = M_\infty^m$ with $\{n, m\} \in \mathbb{Z}^2$. Different values for the pair $\{n, m\}$ are investigated. It is also noted that having $n = m$ is equivalent to setting the viscosity coefficients μ and κ equal. The objective of this investigation is to make a choice on the scaling of the Reynolds and Prandtl numbers, obtain the corresponding asymptotic equations, and determine whether or not the low Mach asymptotic limit is preserved. Since the Reynolds and Prandtl numbers are function of the viscosity coefficients and thus, of the normalization parameter $n(P)$ defined in Eq. (10), a scaling for the function $n(P)$ will be derived as well.

- $Re_\infty = Pr_\infty = 1$ or $m = n = 0$:

Using the assumption $m = n = 0$, the system of equation given in Eq. (15) becomes:

$$\left\{ \begin{array}{l} \partial_t \rho + \nabla \cdot (\rho \vec{u}) \\ \partial_t (\rho \vec{u}) + \nabla \cdot (\rho \vec{u} \otimes \vec{u}) + \frac{1}{M_\infty^2} \nabla (P) \\ \partial_t (\rho E) + \nabla \cdot [\vec{u} (\rho E + P)] \\ + M_\infty^2 \nabla \cdot (\kappa u^2 \nabla \rho) \\ P = (\gamma - 1) (\rho E + M_\infty^2 \rho u^2) \end{array} \right. = \begin{array}{l} \nabla \cdot (\kappa \nabla \rho) \\ \nabla (\rho \mu \nabla^s \vec{u}) + \nabla \cdot (\vec{u} \otimes \kappa \nabla \rho) \\ \nabla \cdot (\kappa \nabla (\rho e)) + M_\infty^2 \nabla \cdot (\vec{u} \rho \mu \nabla^s \vec{u}) \end{array} \quad (15)$$

334

The following asymptotic equations are obtained:

At order M_∞^{-2} :

$$\vec{\nabla} P_0 = 0$$

At order M_∞^{-1} :

$$\vec{\nabla} P_1 = 0$$

At order 1:

$$\begin{aligned} \partial_t \rho_0 &+ \vec{\nabla} \cdot (\rho_0 \vec{u}_0) = \vec{\nabla} \cdot (\kappa_0 \vec{\nabla} \rho_0) \\ \partial_t (\rho_0 \vec{u}_0) &+ \vec{\nabla} \cdot (\rho_0 \vec{u}_0 \otimes \vec{u}_0) + \vec{\nabla} P_2 = \vec{\nabla} \cdot (\rho_0 \mu_0 \vec{\nabla}^s \vec{u}_0 + \kappa_0 \vec{u}_0 \otimes \vec{\nabla} \rho_0) \\ \partial_t (\rho_0 E_0) &+ \vec{\nabla} \cdot [\vec{u}_0 (\rho_0 E_0 + P_0)] = \vec{\nabla} \cdot (\kappa_0 \vec{\nabla} (\rho_0 e_0)) \end{aligned}$$

335

336

337

338

339

340

341

342

From the first two asymptotic equations, it is concluded that the leading- and first-order pressure are constant in space. Thus, the pressure fluctuation will be of order to the Mach number square as required: $P(\vec{x}, t) = P_0(t) + M_\infty^2 \cdot P_2(\vec{x}, t)$ where P_1 subsumed in P_0 . It remains to investigate how the velocity fluctuations scale as a function of the Mach number. Using the equation of state to relate the leading-order pressure to the total and internal energy, the first-order energy equation can be recast as follows:

$$(\gamma - 1) \partial_t P_0 + \gamma \vec{\nabla} \cdot (\vec{u}_0 P_0) = (\gamma - 1) \vec{\nabla} \cdot (\kappa_0 \vec{\nabla} P_0) \quad (16)$$

343

Remembering that $\vec{\nabla} P_0 = 0$, Eq. (16) becomes:

$$-\frac{1}{\gamma P_0} \frac{dP_0}{dt} = \vec{\nabla} \cdot \vec{u}_0 \quad (17)$$

344

345

346

347

348

349

350

351

352

that degenerates into the classical divergent constraint for incompressible flow, $\vec{\nabla} \cdot \vec{u}_0 = 0$, when assuming a constant background pressure P_0 or at steady-state. Thus, at steady-state, the velocity fluctuations will be of the order of the Mach number.

The above results show that the choice $Re_\infty = Pr_\infty = 1$ conserves the low Mach asymptotic limit. Thus, it remains to determine the scaling of the normalization parameter $n(P)$. In the case under consideration, the viscosity coefficients μ and κ are set equal. Using the definition of the viscosity coefficient in Eq. (10) it can be shown that:

$$\mu_\infty = \frac{\rho_\infty c_\infty^2 u_\infty L}{n_{P,\infty}} \quad (18)$$

353

354

355

where $n_{P,\infty}$ is the far-field quantity for the normalization parameter n_P . Substituting Eq. (18) into Eq. (13) and remembering that the numerical Reynolds number scales as one by assumption, it yields:

$$n_{P,\infty} = \rho_\infty c_\infty^2 \quad (19)$$

356

357

Eq. (19) tells us that in the asymptotic limit, the normalization parameter n_P scales as $\rho_\infty c_\infty^2$ which leaves us with two options: either $n_P = \rho c^2$ or

358 $n_P = P$. The choice was made to use $n_P = \rho c^2$ in the low Mach asymptotic
 359 limit: it was found to behave well and the pressure can become locally
 360 negative and null in some particular case as shown in Section 5.

- 361 • $Re_\infty = Pr_\infty = M_\infty$ or $m = n = 1$:
 362 The reasoning leading to the derivation of the asymptotic equations is
 363 similar to the previous case. Thus, only the mains step are given. The
 364 asymptotic equations obtained with the condition $Re_\infty = Pr_\infty = M_\infty$ are
 365 the following:

At order M_∞^{-2} :

$$\vec{\nabla} P_0 = 0$$

At order M_∞^{-1} :

$$\vec{\nabla} P_1 = \vec{\nabla} \cdot (\mu_0 \rho_0 \vec{\nabla}^s \vec{u}_0 + \kappa_0 \vec{u}_0 \vec{\nabla} \rho_0)$$

At order 1:

$$\begin{aligned} \partial_t \rho_0 &+ \vec{\nabla} \cdot (\rho_0 \vec{u}_0) = \vec{\nabla} \cdot (\kappa \vec{\nabla} \rho)_1 \\ \partial_t (\rho_0 \vec{u}_0) &+ \vec{\nabla} \cdot (\rho_0 \vec{u}_0 \otimes \vec{u}_0) + \vec{\nabla} P_2 = \vec{\nabla} \cdot (\rho \mu \vec{\nabla}^s \vec{u} + \kappa \vec{u} \otimes \vec{\nabla} \rho)_1 \\ \partial_t (\rho_0 E_0) &+ \vec{\nabla} \cdot [\vec{u}_0 (\rho_0 E_0 + P_0)] = \vec{\nabla} \cdot (\kappa \vec{\nabla} (\rho e))_1 \end{aligned}$$

366 Unlike the previous case, only the leading-order pressure P_0 is spatially
 367 constant. Thus, the pressure fluctuations are expected to be of the order
 368 of the Mach number instead of the Mach number square as predicted:
 369 $P(\vec{x}, t) = P_0(t) + M_\infty P_1(\vec{x}, t) + M_\infty^2 P_2(\vec{x}, t)$. Using the equation of state,
 370 the order 1 of the energy equation can be recast as follows:

$$(\gamma - 1) \partial_t P_0 + \gamma P_0 \vec{\nabla} \cdot \vec{u}_0 = (\gamma - 1) \vec{\nabla} \cdot (\kappa_0 \vec{\nabla} P_1) \quad (20)$$

371 Thus, at steady-state, in the presence of pressure fluctuation in the first-
 372 order pressure P_1 , the divergence constraint from the asymptotic analysis
 373 $\vec{\nabla} \cdot \vec{u}_0 = 0$ is not satisfied. By choosing the Reynolds and Prandtl numbers
 374 equal to the Mach number, the multi-D Euler equations do not seem to
 375 converge to the incompressible equations in the low Mach asymptotic limit.
 376 The scaling of the normalization parameters that matches the condition
 377 $Re_\infty = Pr_\infty = M_\infty$ is derived on the same model as before:

$$n_{P,\infty} = \rho_\infty u_\infty c_\infty \quad (21)$$

378 which imposes $n(P) = \rho c \|\vec{u}\|$.

- 379 • $Re_\infty = M_\infty$ and $Pr_\infty = 1$ or $m = 1$ and $n = 0$:
 380 For this particular case, the viscosity coefficients μ and κ are not set equal.
 381 Therefore, two normalization parameters have to be determined. The
 382 details of the derivation are given in appendix (not done yet). The correct
 383 low Mach asymptotic limit was recovered with the choice $Re_\infty = M_\infty$ and
 384 $Pr_\infty = 1$.

385 This normalization parameter is only valid in the asymptotic limit and the
 386 purpose of this paper is to define a viscosity coefficient μ that is valid for a wide
 387 range of Mach numbers. Thus, it is proposed to define the high-order viscosity
 388 coefficient μ_e as follows:

$$\mu_e = h^2 \frac{\max(\tilde{D}_e, J)}{(1 - f(M))g(P) + f(M)\rho||\vec{u}||^2} \quad (22)$$

389 where $f(M)$ is a function of the local Mach number M with the following prop-
 390 erties:

$$\begin{cases} f(M) \rightarrow 0 \text{ as } M \rightarrow 0 \\ f(M) \rightarrow 1 \text{ as } M \geq 1 \end{cases} \quad (23)$$

391 and $g(P)$ has the following definition:

$$\begin{cases} g(P) = \rho c^2 \text{ if } Re_\infty = Pr_\infty = 1 \\ g(P) = \rho c ||\vec{u}|| \text{ if } Re_\infty = Pr_\infty = M_\infty \end{cases} \quad (24)$$

392 The choice of the function $f(M)$ is not fixed and a few examples are available
 393 in the literature. A simple definition is $f(M) = \min(M, 1)$ which meets the
 394 conditions of Eq. (23). Another definition for $f(M)$ was proposed by [12].
 395 All of the numerical results presented in Section 5 were obtained by using
 396 $f(M) = \min(M, 1)$ which is simple to implement. A convergence test for a
 397 subsonic flow over a 2-D cylinder will show that this definition of $f(M)$ yields
 398 the correct behavior in the asymptotic limit. The definition of the high-order
 399 viscosity coefficient $\mu_e(\vec{r}, t)$ should behave well for complex flow where a near
 400 incompressible regime coexists with a supersonic flow domain since $f(M)$ is
 401 function of the local Mach number.

402 For clarity purpose, the full definition of the viscosity coefficient $\mu(\vec{r}, t)$ is re-
 403 called:

$$\begin{cases} \mu(\vec{r}, t) = \max(\mu_{max}(\vec{r}, t), \mu_e(\vec{r}, t)) \\ \text{where } \mu_{max}(\vec{r}, t) = \frac{h}{2} (||\vec{u}|| + c) \\ \text{and } \mu_e(\vec{r}, t) = h^2 \frac{\max(\tilde{D}_e, J)}{(1 - f(M))g(P) + f(M)\rho||\vec{u}||^2} \\ \mu(\vec{r}, t) = \kappa(\vec{r}, t) \end{cases} \quad (25)$$

404 These viscosity coefficients are valid for both the multi-D Euler equations with
 405 variable and constant area and are employed with the dissipative terms detailed
 406 in Eq. (15). The reader will notice that, through the derivation, none assumption
 407 was made on the type of equation of state besides the convexity condition on
 408 the entropy function s . The remaining of this paper (Section 5) will focus on
 409 demonstrating that the definition of the viscosity coefficient given in Eq. (25) is
 410 indeed well-scaled in the asymptotic limit and that shocks are still well resolved.

411 4. Solution Techniques Spatial and Temporal Discretizations

412 In order to detail the partial and temporal discretization used for this study,
 413 the system of equations Eq. (7) is considered under the following form for sim-
 414 plicity: **no $\vec{\nabla} \cdot D(U) \vec{\nabla} U$ term here to represent the viscous regularization?**

$$\partial_t U + \vec{\nabla} \cdot F(U) = S \quad (26)$$

where U is the vector solution, F is a conservative vector flux and S is a vector source that can contain the non-conservative term $P\vec{\nabla}A$.

4.1. Spatial and Temporal Discretizations

The system of equation given in Eq. (26) is discretized using a continuous Galerkin finite element method and high-order temporal integrators provided by the MOOSE framework.

4.1.1. CFEM

In order to apply the continuous finite element method, Eq. (26) is multiplied by a smooth test function ϕ , integrated by parts and each integral is split onto each finite element e of the discrete mesh Ω bounded by $\partial\Omega$, to obtain a weak solution:

$$\sum_e \int_e \partial_t U \phi - \sum_e \int_e F(U) \cdot \vec{\nabla} \phi + \int_{\partial\Omega} F(U) \vec{n} \phi - \sum_e \int_e S \phi = 0 \quad (27)$$

The integrals over the elements e are evaluated using quadrature-point rules. The Moose framework provides a wide range of test function and quadrature rules: trapezoidal and Gauss rules among others. Linear Lagrange polynomials will be used as test functions and should ensure second-order convergence for smooth functions. The order of convergence will be demonstrated.

4.1.2. Temporal integrator

The MOOSE framework offers both first- and second-order explicit and implicit temporal integrators. In all of the numerical examples presented in Section 5, the time-dependent term $\int_e \partial_t U \phi$ will be evaluated using the second-order temporal integrator BDF2. By considering three solutions, U^{n-1} , U^n and U^{n+1} at three different times t^{n-1} , t^n and t^{n+1} , respectively, it yields:

$$\begin{aligned} \int_e \partial_t U \phi &= \int_e (\omega_0 U^{n+1} + \omega_1 U^n + \omega_2 U^{n-1}) \phi \\ \text{with } \omega_0 &= \frac{2\Delta t^{n+1} + \Delta t^n}{\Delta t^{n+1} (\Delta t^{n+1} + \Delta t^n)}, \\ \omega_1 &= -\frac{\Delta t^{n+1} + \Delta t^n}{\Delta t^{n+1} \Delta t^n} \\ \text{and } \omega_2 &= \frac{\Delta t^{n+1}}{\Delta t^n (\Delta t^{n+1} + \Delta t^n)} \end{aligned} \quad (28)$$

where $\Delta t^n = t^n - t^{n-1}$ and $\Delta t^{n+1} = t^{n+1} - t^n$.

4.2. Boundary conditions

The boundary conditions will be treated by either using Dirichlet or Neumann conditions. The multi-D Euler equations are wave-dominated systems that require great care when dealing with boundary conditions. It is often recommended to use the characteristic equations to compute the correct flux at the

boundaries. Our implementation of the subsonic boundary conditions will follow the method described in [19] that was developed for Ideal Gas and Stiffened Gas equation of states. For each numerical solution presented in Section 5, the type of boundary conditions used will be specified and taken among the followings: supersonic inlet, subsonic inlet (stagnation pressure boundary), supersonic outlet and subsonic inlet (static pressure boundary).

4.3. Solver

A Free-Jacobian-Newton-Krylov (FJNK) method is used to solve for the solution at each time step. The jacobian matrix of the discretized equations was derived by hand, hard coded and used as a preconditioner. This method requires the partial derivative of the pressure with respect to the conservative variables to be known. The contribution of the artificial dissipative terms to the jacobian matrix is simplified by assuming constant viscosity coefficients as shown in Eq. (29) for the dissipative terms of the continuity equation:

$$\frac{\partial}{\partial U_i} \left(\kappa \vec{\nabla} \rho \vec{\nabla} \phi \right) = \kappa \frac{\partial}{\partial U_i} (\rho) \vec{\nabla} \phi \quad (29)$$

where U_i denotes the set of conservative variables.

5. Numerical Results

make sure you give the Mach number for the various problems

This section is dedicated to presenting 1- and 2-D numerical results obtained by solving Eq. (7) with the entropy viscosity method. This section has two objectives: validate our new definition of the viscosity coefficients for the low Mach limit, and, make sure that the new definition can still resolve shocks.

The first set of 1-D simulations consist of liquid water and steam flowing in a convergent-divergent nozzle. This test is interesting for multiple reasons: a steady-state is reached (some stabilization methods are known to have difficulties to reach a steady-state ([3, 4]), it can be performed for liquid and gas phases, and, an analytical solution of the steady-state solution is available which allow for convergence study. The 1-D Leblanc shock tube test [21] (in a straight pipe) is also performed and consists of a flow developing shocks. A convergence study will be performed in order to demonstrate convergence of the numerical solution to the exact solution.

This section also included 2-D simulations from subsonic to supersonic flows. Subsonic flows of a gas over a 2-D cylinder and a hump [22] are simulated and results are shown for various far-field Mach numbers. Numerical results of a supersonic flow in a compression corner are provided to illustrate the capabilities of the new definition in the supersonic case. Convergence studies are performed when an analytical solution is available.

For each simulation, informations relative to the boundary conditions and the equation of state will be provided. All of the numerical solution presented in

481 this section are run with the second-order temporal integrator *BDF2* and lin-
482 ear polynomials test functions. The integrals are numerically computed using
483 a second-order Gauss quadrature rule. The Ideal Gas [23] or Stiffened Gas
484 equation of state [24] are used and a generic formulation is recalled in Eq. (30).

$$P = (\gamma - 1)\rho(e - q) - \gamma P_\infty \quad (30)$$

485 where the parameters q and P_∞ are fluid dependent and will be specified in time.
486 Eq. (30) degenerates to the Ideal Gas equation of state by setting q and P_∞ to
487 zero. The Ideal and Stiffened Gas equation of states have a convex entropy s :

$$s = C_v \ln \left(\frac{P + P_\infty}{\rho^{\gamma-1}} \right)$$

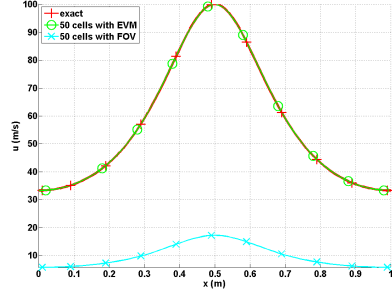
488 5.1. Liquid water in a 1-D divergent-convergent nozzle

489 The simulation consists of liquid water flowing through a 1-D convergent-
490 divergent nozzle with the following equation, $A(x) = 1 + 0.5 \cos(2\pi x/L)$, where
491 $L = 1m$ is the length of the nozzle. At the inlet, the stagnation pressure and
492 temperature are set to $P_0 = 1MPa$ and $T_0 = 453K$, respectively. At the
493 outlet, only the static pressure is specified: $P_s = 0.5MPa$. Details about the
494 theory related to the inlet and outlet boundary conditions can be found in [19].
495 Initially, the temperature is uniform and set equal to the stagnation temperature
496 and the pressure linearly decreases from the stagnation pressure to the static
497 one. Finally, the liquid is assumed at rest. The Stiffened Gas equation of state
498 is used to model the liquid water with the parameters provided in Table 1.

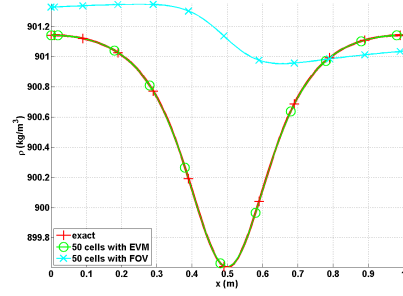
Table 1: Stiffened Gas Equation of State parameters for liquid water.

γ	$C_v (J \cdot kg^{-1} \cdot K^{-1})$	$P_\infty (Pa)$	$q (J \cdot kg^{-1})$
2.35	1816	10^9	-1167.10^3

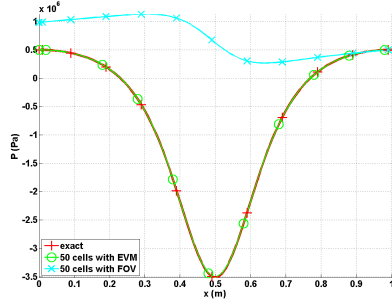
499 Because of the low pressure difference between the inlet and the outlet,
500 and the large value of P_∞ , the flow remains subsonic and thus, should not
501 display any shock. Enthalpy and entropy are conserved through the nozzle,
502 and these conservation relations are used to determine the exact solution at
503 steady-state [25]. Plots of the velocity, density and pressure are given at steady-
504 state in Fig. 1a, Fig. 1b, Fig. 1c, respectively, along with the exact solution for
505 comparison. The viscosity coefficients are also plotted in Fig. 1d. The mesh
506 used is uniform and has 50 cells.



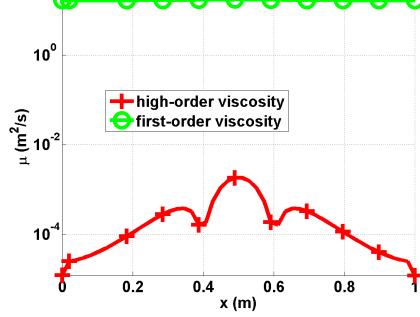
(a) Velocity solution at steady-state.



(b) Density solution at steady-state.



(c) Pressure solution at steady-state.



(d) Viscosity coefficients at steady-state.

Figure 1: Steady-state solution for liquid phase in a 1-D convergent-divergent nozzle with an uniform mesh of 50 cells.

In Fig. 1, the numerical solutions of the pressure, velocity and density obtained with the first-order viscosity (FOV) and the entropy viscosity method (EVM) are plotted against the exact solution. A fairly coarse mesh (50 cells) was used. The numerical solution obtained with the EVM and the exact solution perfectly overlap. On the other hand, the numerical solution run with the FOV does not give the correct steady-state: this is an illustration of the effect of ill-scaled dissipative terms. It is also noted that the second-order viscosity coefficient is very small compare to the first-order one as expected (Fig. 1d): (i) the numerical solution is smooth as shown in Fig. 1 and (ii) the flow is in a low Mach regime and thus isentropic. A convergence study was performed using the exact solution as a reference: the L1 and L2 norms of the error and the corresponding convergence rates are computed at steady-state on various uniform mesh from 4 to 256 cells. The results for linear polynomials Q_1 are reported in Table 2 and Table 3 for the primitive variables: density, velocity and pressure.

Table 2: L1 norm of the error for the liquid phase in a 1-D convergent-divergent nozzle at steady-state.

cells	density	rate	pressure	rate	velocity	rate
4	$2.8037 \cdot 10^{-1}$	—	$8.4705e \cdot 10^5$	—	7.2737	—
8	$1.3343 \cdot 10^{-1}$	1.0713	$4.7893e \cdot 10^5$	0.24227	6.1493	0.074683
16	$2.9373 \cdot 10^{-2}$	2.1835	$1.0613e \cdot 10^5$	2.3247	1.2275	2.4501
32	$5.1120 \cdot 10^{-3}$	2.5225	$1.8446 \cdot 10^4$	2.6959	$1.8943 \cdot 10^{-1}$	3.0966
64	$1.0558 \cdot 10^{-3}$	2.2755	$3.7938 \cdot 10^3$	2.3207	$3.7919 \cdot 10^{-2}$	2.3323
128	$2.3712 \cdot 10^{-4}$	2.1547	$8.4471 \cdot 10^2$	2.0624	$8.5517 \cdot 10^{-3}$	2.0473
256	$5.6058 \cdot 10^{-5}$	2.0806	$1.9839 \cdot 10^2$	2.0478	$2.0475 \cdot 10^{-3}$	1.9833
512	$1.3278 \cdot 10^{-5}$	2.0778	46.622	2.0478	$4.9516 \cdot 10^{-4}$	1.9669

Table 3: L2 norm of the error for the liquid phase in a 1-D convergent-divergent nozzle at steady-state.

cells	density	rate	pressure	rate	velocity	rate
4	$3.106397 \cdot 10^{-1}$	—	$5.254445 \cdot 10^5$	—	3.288543	—
8	$7.491623 \cdot 10^{-2}$	2.07	$1.636966 \cdot 10^5$	1.60	1.823880	0.90
16	$2.079858 \cdot 10^{-2}$	1.80	$4.627338 \cdot 10^4$	1.75	$4.990605 \cdot 10^{-1}$	1.83
32	$5.329627 \cdot 10^{-3}$	1.90	$1.180287 \cdot 10^4$	1.92	$1.261018 \cdot 10^{-1}$	1.93
64	$1.341583 \cdot 10^{-3}$	1.94	$2.967104 \cdot 10^3$	1.98	$3.160914 \cdot 10^{-2}$	1.99
128	$3.359766 \cdot 10^{-4}$	1.99	$7.428087 \cdot 10^2$	1.99	$7.907499 \cdot 10^{-3}$	1.99
256	$8.403859 \cdot 10^{-5}$	1.99	$1.857861 \cdot 10^2$	1.99	$1.977292 \cdot 10^{-3}$	1.99
512	$2.10075 \cdot 10^{-5}$	1.99	27.048	1.99	$4.9516 \cdot 10^{-4}$	1.99

It is observed that the convergence rate for the L1 and L2 norm of the error is 2: the entropy viscosity method conserves the high-order accuracy when the numerical solution is smooth, and the new definition of the entropy viscosity coefficient seems to behave as expected in the low Mach limit.

5.2. Steam in a 1-D divergent-convergent nozzle

Instead of liquid water, we now simulate a flow of steam using the exact same 1-D geometry, initial conditions and boundary conditions as in Section 5.1. The Stiffened gas equation of state is still used but with different parameters that are given in Table 4: steam is a gas and compressible effects will become dominant.

Table 4: Stiffened Gas Equation of State parameters for steam.

γ	$C_v (J \cdot kg^{-1} \cdot K^{-1})$	$P_\infty (Pa)$	$q (J \cdot kg^{-1})$
1.43	1040	0	$2030 \cdot 10^3$

531 The pressure difference applied between the inlet and outlet is large enough
 532 to make the steam accelerates through the nozzle and result in the formation of
 533 shock in the divergent part. The behavior is different from what is observed for
 534 the liquid water phase in Section 5.1 because of the liquid to gas density ratio
 535 that is of 1000. Even though a shock forms, an exact solution at steady-state
 536 is still available [25]. The objective of this section is to show that using the
 537 new definition of the viscosity coefficient in Eq. (25), the shock can be correctly
 538 resolved without spurious oscillation. The steady-state numerical solution is
 539 shown in Fig. 2 and was run with a mesh of 1600 cells.

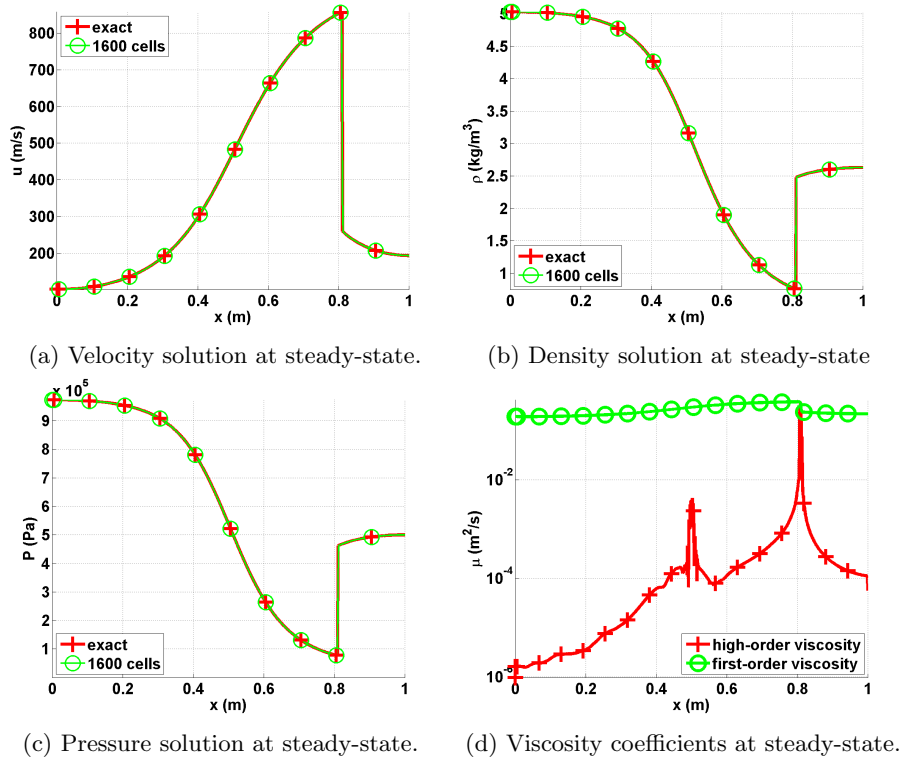


Figure 2: Steady-state solution for vapor phase in a 1-D convergent-divergent nozzle.

540 The steady-state solution of the density, velocity and pressure are given
 541 in Fig. 2a, Fig. 2b and Fig. 2c. The steady-solution displays a shock around
 542 $x = 0.8m$ and match the exact solution. In Fig. 2d, the first- and second-
 543 order viscosity coefficients are log plotted at steady-state: the second-order
 544 viscosity coefficient is peaked in the shock region around $x = 0.8m$ as expected,
 545 and saturate to the first-order viscosity coefficient. The profile also displays
 546 another peak at $x = 0.5m$ that corresponds to the position of the sonic point
 547 for a 1-D convergent-divergent nozzle: this particular point is known to develop
 548 small instabilities that are detected when computing the jumps of the pressure

and density gradients. Anywhere else, the second-order viscosity coefficient is small. In order to prove convergence of the numerical solution to the exact solution, a convergence study is performed. Because of the presence of a shock, second-order accuracy cannot be achieved. However, the convergence rate of a numerical solution containing a shock is known and expected to be of 1 and 1/2 when computing the L1 and L2 norms of the error, respectively (see Theorem 9.3 in [26]). Results are reported in Table 5 and Table 6 for the primitive variables: density, velocity and pressure.

Table 5: L1 norm of the error for the vapor phase in a 1-D convergent-divergent nozzle at steady-state.

cells	density	rate	pressure	rate	velocity	rate
5	$0.72562 \cdot 10^{-1}$	—	$1.5657 \cdot 10^5$	—	173.69	—
10	$0.4165 \cdot 10^{-1}$	0.80088	$9.6741 \cdot 10^4$	0.63425	120.69	0.52519
20	$0.20675 \cdot 10^{-1}$	1.0104	$4.9193 \cdot 10^4$	0.96971	72.149	0.74228
40	$0.093703 \cdot 10^{-1}$	1.1417	$2.0103 \cdot 10^4$	0.72728	34.716	1.0554
80	$0.047328 \cdot 10^{-1}$	0.9854	$1.0208 \cdot 10^4$	0.9777	16.082	1.1101
160	$0.023965 \cdot 10^{-2}$	0.9817	$5.1969 \cdot 10^3$	0.9739	7.9573	1.0150
320	$0.020768 \cdot 10^{-2}$	0.9886	$2.5116 \cdot 10^3$	1.0490	3.7812	1.0734
640	$0.0059715 \cdot 10^{-2}$	1.0160	$1.2754 \cdot 10^3$	0.9776	1.8353	1.0428

Table 6: L2 norm of the error for the vapor phase in a 1-D convergent-divergent nozzle at steady-state.

cells	density	rate	pressure	rate	velocity	rate
5	$9.7144 \cdot 10^{-1}$	—	$2.0215 \cdot 10^5$	—	236.94	—
10	$5.9718 \cdot 10^{-1}$	0.70195	$1.3024 \cdot 10^5$	0.63425	166.56	0.50854
20	$2.9503 \cdot 10^{-1}$	1.0173	$6.6503 \cdot 10^4$	0.96971	103.36	0.68831
40	$1.8193 \cdot 10^{-1}$	0.69747	$4.0171 \cdot 10^4$	0.72728	66.374	0.6390
80	$1.3366 \cdot 10^{-1}$	0.44485	$2.3163 \cdot 10^4$	0.43576	42.981	0.62692
160	$9.6638 \cdot 10^{-2}$	0.46790	$1.7263 \cdot 10^4$	0.42413	31.717	0.43844
320	$7.0896 \cdot 10^{-2}$	0.44688	$1.2763 \cdot 10^4$	0.43571	23.138	0.45499
640	$5.2191 \cdot 10^{-2}$	0.44190	$9.4217 \cdot 10^3$	0.43790	16.910	0.45238

The convergence rates for the L1 and L2 norms of the error are close to the theoretical values which prove convergence of the numerical solution to the exact solution.

5.3. Leblanc shock tube

The 1-D Leblanc shock tube is a Riemann problem designed to test the robustness and the accuracy of the stabilization method. The initial conditions

are given in Table 7. The ideal gas equation of state is used to compute the fluid pressure with the following heat capacity ratio $\gamma = 5/3$.

Table 7: Initial conditions for the 1-D Leblanc shock tube.

	ρ	u	e
left	1.	0.	0.1
right	10^{-3}	0.	10^{-7}

This test is computationally challenging because of the large left to right pressure ratio. The computational domain consists of a 1-D pipe of length $L = 9m$ with an interface located at $x = 2m$. At $t = 0.s$, the interface is removed, allowing the fluid to move. The numerical solution is run until $t = 4.s$ and the density, momentum and total energy profiles are given in Fig. 3a, Fig. 3b and Fig. 3c, respectively, along with the exact solution. The viscosity coefficients are also plotted in Fig. 3d. These plots were run with three different uniform mesh of 800, 3200 and 6000 cells and a constant time step $\Delta t = 10^{-3}s$.

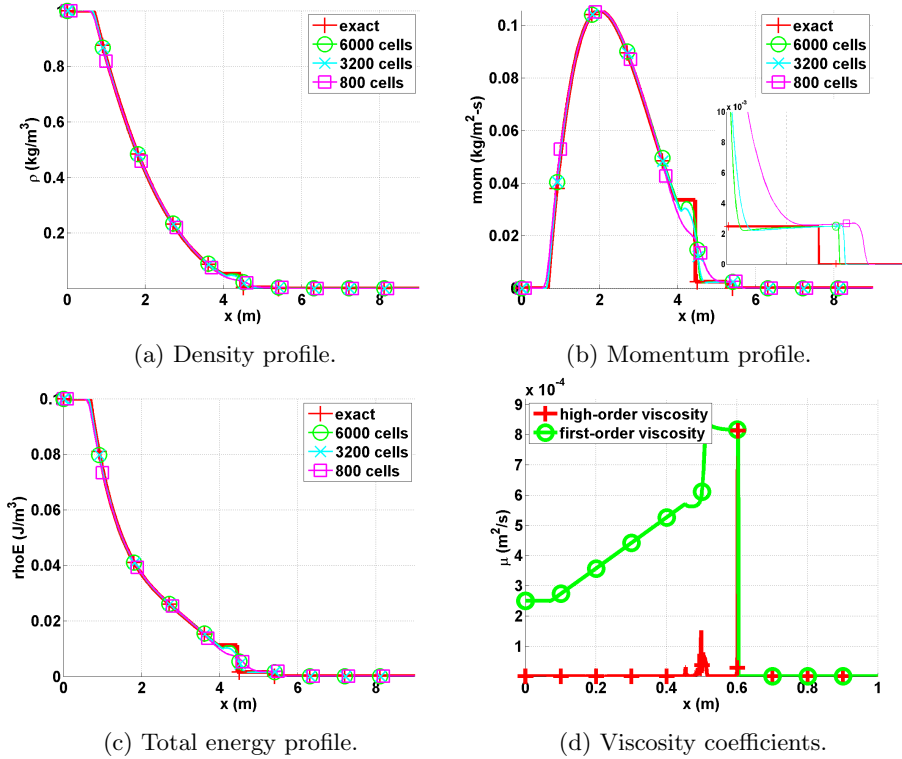


Figure 3: Numerical solution for the 1-D Leblanc shock tube at $t = 4.s$.

573 The density, momentum and total energy profiles given in Fig. 3 do not
 574 display any oscillations. In Fig. 3b, the shock region is zoomed in for better
 575 resolution: the shock is well resolved and do not show any oscillation. It is
 576 also observed that the shock position of the numerical solution converges to the
 577 exact position when refining the mesh. The contact wave is shown in Fig. 3b at
 578 $x = 4.5m$. The second-order viscosity coefficient profile is shown in Fig. 3d and
 579 behaves as expected: it saturates to the first-order viscosity in the shock region
 580 and thus prevent oscillations from forming. In the contact wave at $x = 4.5m$, a
 581 smaller peak is observed that is due to the presence of the jumps in the definition
 582 of the second-order viscosity coefficient (Eq. (25)).
 583 Once again, a convergence study is performed in order to prove convergence of
 584 the numerical solution to the exact solution. As for the vapor phase in the 1-D
 585 nozzle (Section 5.2), the expected convergence rate for the L1 and L2 norms
 586 of the error are 1 and 1/2, respectively. The exact solution was obtained by
 587 running a 1-D Riemann solver and used as a reference solution to compute the
 588 L1 and L2-norms of the error that are reported in Table 8 and Table 9 for the
 589 conservative variables: density, momentum and total energy.

Table 8: L1 norm of the error for the 1-D Leblanc test at $t = 4.s$.

cells	density	rate	momentum	rate
100	$1.0354722 \cdot 10^{-2}$	—	$3.5471714 \cdot 10^{-3}$	—
200	$7.2680512 \cdot 10^{-3}$	0.51064841	$2.5933119 \cdot 10^{-3}$	0.45187331
400	$5.0825628 \cdot 10^{-3}$	0.51601245	$2.0668092 \cdot 10^{-3}$	0.32739054
800	$3.4025056 \cdot 10^{-3}$	0.57895861	$1.4793838 \cdot 10^{-3}$	0.48240884
1600	$2.1649953 \cdot 10^{-3}$	0.65223363	$9.7152832 \cdot 10^{-4}$	0.60666684
3200	$1.2465433 \cdot 10^{-3}$	0.79643094	$5.5937409 \cdot 10^{-4}$	0.79644263
6400	$6.4476928 \cdot 10^{-4}$	0.95107804	$3.0244198 \cdot 10^{-4}$	0.88715502
12800	$3.3950948 \cdot 10^{-4}$	0.92533116	$1.5958118 \cdot 10^{-4}$	0.9223679

cells	total energy	rate
100	0.0014033046	—
200	$9.8611746 \cdot 10^{-4}$	0.5089968
400	$7.7844421 \cdot 10^{-4}$	0.34116585
800	$5.5702549 \cdot 10^{-4}$	0.48285029
1600	$3.5720171 \cdot 10^{-4}$	0.64100438
3200	$2.0491799 \cdot 10^{-4}$	0.80169235
6400	$1.0914891 \cdot 10^{-4}$	0.90874889
12800	$5.7909794 \cdot 10^{-5}$	0.91441847

Table 9: L2 norm of the error for the 1-D Leblanc test at $t = 4.s$.

cells	density	rate	momentum	rate
100	$5.7187851 \cdot 10^{-3}$	—	$1.7767236 \cdot 10^{-3}$	—
200	$3.8995238 \cdot 10^{-3}$	0.55241073	$1.4913161 \cdot 10^{-3}$	0.25263314
400	$2.8103526 \cdot 10^{-3}$	0.4725468	$1.3305301 \cdot 10^{-3}$	0.164585
800	$2.1081933 \cdot 10^{-3}$	0.41474398	$1.1398931 \cdot 10^{-3}$	0.22310254
1600	$1.5731052 \cdot 10^{-3}$	0.42239201	$9.0394227 \cdot 10^{-4}$	0.33459602
3200	$1.0610667 \cdot 10^{-3}$	0.56809979	$6.2735595 \cdot 10^{-4}$	0.52694639
6400	$7.3309974 \cdot 10^{-4}$	0.53343397	$4.4545754 \cdot 10^{-4}$	0.49399631
12800	$5.1020991 \cdot 10^{-4}$	0.52291857	$3.1266758 \cdot 10^{-4}$	0.5106583

cells	total energy	rate
100	$7.6112265 \cdot 10^{-4}$	—
200	$5.5497308 \cdot 10^{-4}$	0.45571115
400	$4.6063172 \cdot 10^{-4}$	0.26880405
800	$3.7798953 \cdot 10^{-4}$	0.28526749
1600	$2.9584646 \cdot 10^{-4}$	0.35349763
3200	$2.054455 \cdot 10^{-4}$	0.52609289
6400	$1.4670834 \cdot 10^{-4}$	0.48580482
12800	$1.0299897 \cdot 10^{-5}$	0.51032105

The convergence rates are close to the expected values which prove convergence of the numerical solution to the exact solution.

5.4. Subsonic flow over a 2-D cylinder

The flow of a fluid over a 2-D cylinder is a typical benchmark case to test the behavior of a numerical method in the low Mach regime. For this test, an analytical solution is available in the incompressible limit or low Mach limit (REFS) and often referred to as potential flow. The main features of the potential flow are the following:

- The solution is symmetric: the iso-mach number lines are used to assess the symmetry of the numerical solution.
- The velocity at the top of the cylinder is twice the incoming velocity set at the inlet.
- The pressure fluctuations are proportional to the inlet Mach number square, as follows:

$$\tilde{P} = \frac{\max(P) - \min(P)}{\max(P)} \propto M_{\infty}^2$$

where \tilde{P} and M_{∞} are the pressure fluctuations and the inlet Mach number, respectively.

606 The computational domain consists of a 1×1 square with a circular hole of radius
 607 0.05 in its middle. At the inlet, a subsonic stagnation boundary condition is
 608 used: the stagnation pressure and temperature are computed using the following
 609 relations, valid for the Stiffened and Ideal gas equation of states:

$$\begin{cases} P_0 = P \left(1 + \frac{\gamma-1}{2} M^2\right)^{\frac{\gamma}{\gamma-1}} \\ T_0 = T \left(1 + \frac{\gamma-1}{2} M^2\right) \end{cases} \quad (31)$$

610 The static pressure $P_s = 101325 \text{ Pa}$ is set at the subsonic outlet and a static
 611 pressure boundary type is used. The implementation of the pressure boundary
 612 conditions is done on the model of [19]. A solid wall boundary condition is set for
 613 the top and bottom walls of the computational domain: the normal velocity is
 614 zero since no mass can penetrate the solid body. The mesh is made of triangular
 615 cells.

616 The steady-state for Mach numbers ranging from $M_\infty = 10^{-3}$ to $M_\infty = 10^{-7}$
 617 is shown in Fig. 4. The iso-Mach lines are drawn with 50 intervals ranging from
 618 10^{-8} to $2M_\infty$, and allow to assess the symmetry of the numerical solution.

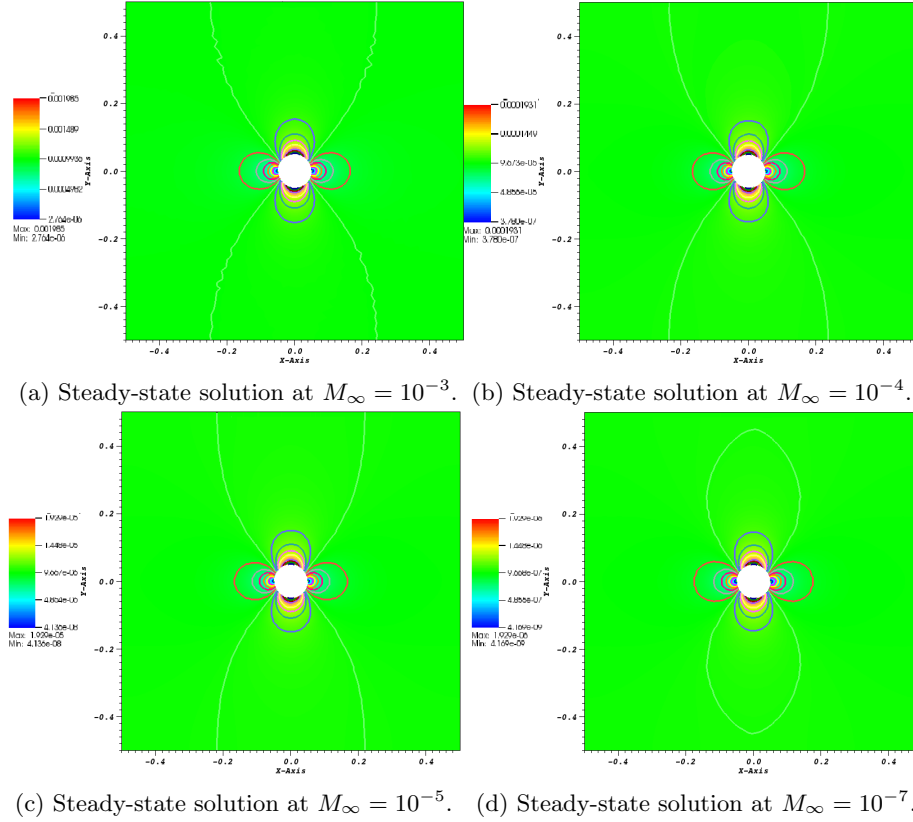


Figure 4: Steady-state solution for a subsonic flow over a 2-D cylinder.

619 In Table 10, the velocity at the top of the cylinder and at the inlet are given
620 for the different values of the Mach number presented in Fig. 4. The ratio of
621 the inlet velocity to the velocity at the top of cylinder is also computed and is
622 very close to 2 as expected.

Table 10: Velocity ratio for different Mach numbers.

Mach number	inlet velocity	velocity at the top of the cylinder	ratio
10^{-3}	$2.348 \cdot 10^{-3}$	$1.176 \cdot 10^{-3}$	1.99
10^{-4}	$2.285 \cdot 10^{-4}$	$1.145 \cdot 10^{-4}$	1.99
10^{-5}	$2.283 \cdot 10^{-5}$	$1.144 \cdot 10^{-5}$	1.99
10^{-6}	$2.283 \cdot 10^{-6}$	$1.144 \cdot 10^{-6}$	1.99
10^{-7}	$2.283 \cdot 10^{-7}$	$1.144 \cdot 10^{-7}$	1.99

623 In Fig. 5, the pressure and velocity fluctuations are plotted as a function
624 of the far field Mach number, on a log-log plot. The pressure and velocity
625 fluctuations are expected to be of the order of the Mach number square and
626 the Mach number, respectively. It is known that some stabilization methods,
627 alike upwind scheme [27], can produce pressure fluctuations with the wrong
628 order. The objective of Fig. 5 is to show that the new definition of the viscosity
629 coefficients yields the correct order in the low Mach limit for both the pressure
630 and velocity variables. For reference purpose, the function $f(M) = M^2$ and
631 $f(M) = M$ are plotted.

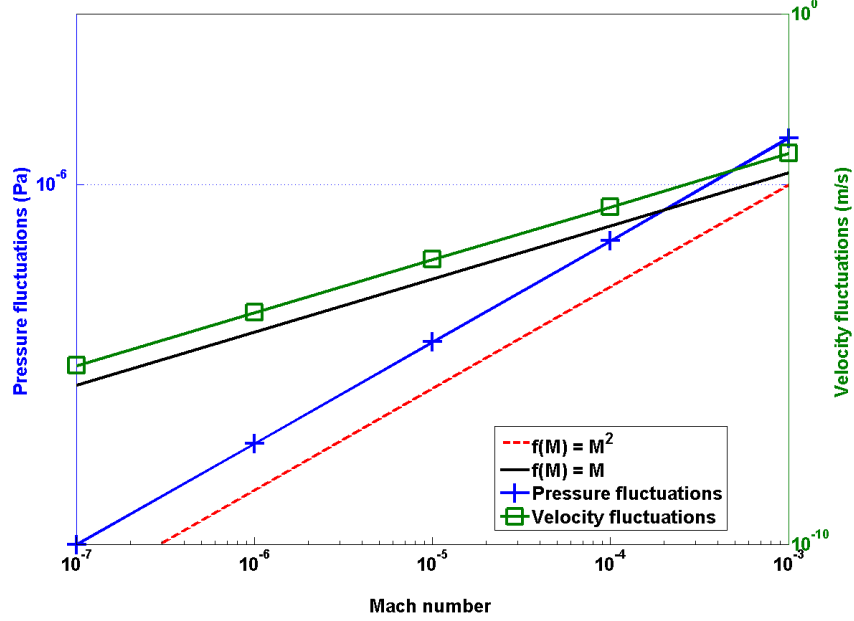


Figure 5: Log-log plot of the pressure and velocity fluctuations as a function of the far field Mach number.

5.5. Subsonic flow over a 2-D hump

This is another example of an internal flow configuration. It consists of a channel of height $L = 1 \text{ m}$ and length $3L$, with a circular bump of length L and thickness $0.1L$. The bump is located on the bottom wall at a distance L from the inlet. The system is initialized with a uniform pressure $P = 101325 \text{ Pa}$ and temperature $T = 300 \text{ K}$. The initial velocity is computed from the Mach number, M_∞ , the pressure, the temperature and the Ideal Gas equation of state with the heat capacity $C_v = 717 \text{ J/kg} \cdot \text{K}$ and the heat capacity ratio $\gamma = 1.4$. At the inlet, a subsonic stagnation boundary condition is used and the stagnation pressure and temperature are computed using Eq. (31). The static pressure $P_s = 101325 \text{ Pa}$ is set at the subsonic outlet. A uniform grid is used to get the numerical solution until steady-state is reached. The results are shown in Fig. 6a, Fig. 6b, Fig. 6c and Fig. 6d for the inlet Mach numbers $M_\infty = 0.7$, $M_\infty = 0.01$, $M_\infty = 10^{-4}$ and $M_\infty = 10^{-7}$, respectively. It is expected that, within the low Mach number range, the solution does not depend on the Mach number and is identical to the solution obtained with an incompressible flow code. On the other hand, for a flow at $M = 0.7$, the compressible effects become more important and shock can form.

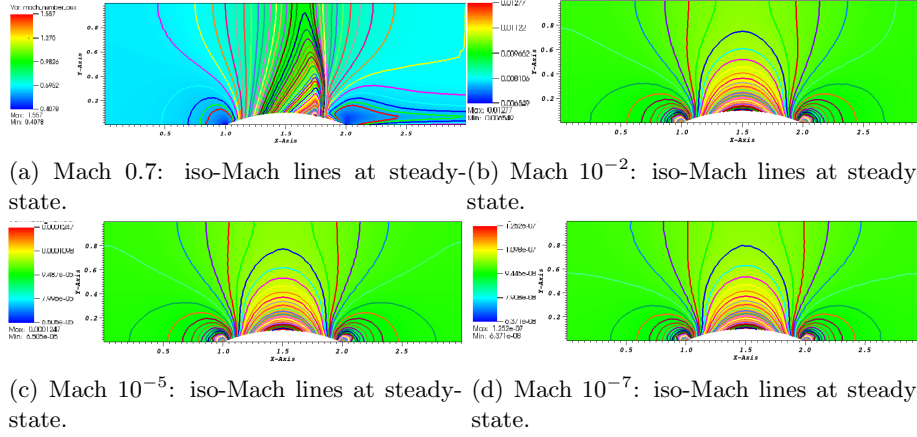


Figure 6: Steady-state solution for a 2-D flow over a circular bump.

650 The results showed in Fig. 6b, Fig. 6c and Fig. 6d correspond to the low
 651 Mach regime. The iso-Mach lines are drawn ranging from the minimum and the
 652 maximum of each legend with 50 intervals. The steady-state solution is sym-
 653 metric and does not depend on the value of the inlet Mach number as expected.
 654 In Fig. 6a, the steady-state numerical solution develops a shock: the compress-
 655 ibility effect are no longer negligible. The iso-Mach lines are also plotted with
 656 50 intervals and ranging from 0.4 to 1.6. The shock is well resolved and does
 657 not display any instability or spurious oscillation.
 658 The results presented in Fig. 6 were obtained with the new definition of the vis-
 659 cosity coefficient (see Eq. (25)), and, illustrate the capabilities of the entropy-
 660 viscosity method to adapt to the type of flow (subsonic and transonic flows)
 661 without using any tuning parameters, but by just evaluating the entropy resid-
 662 ual that is an indicator of the entropy production.

663 5.6. Supersonic flow in a compression corner

664 This is an example of a supersonic flow over a wedge of angle 15° where an
 665 oblique shock is generated at steady-state. The Mach number upstream of the
 666 shock is fixed to $M = 2.5$. The initial conditions are uniform: the pressure and
 667 temperature are set to $P = 101325 \text{ Pa}$ and $T = 300 \text{ K}$, respectively. The initial
 668 velocity is computed from the upstream Mach number and using the Ideal Gas
 669 equation of state with the same parameters as in Section 5.5. The code is run
 670 until steady-state. From the oblique shock theory [14], an analytical solution for
 671 this supersonic flow is available and give the downstream to upstream pressure,
 672 entropy and Mach number ratios. The analytical and numerical ratios are given
 673 in Table 11, and are very close. The shock wave angle at steady-state is also
 674 known and given by the so-called $\theta - \beta - M$ relation:

$$\tan \theta = 2 \cot \beta \frac{M^2 \sin^2 \beta - 1}{M^2 (\gamma + \cos^2(2\beta)) + 2}$$

where θ , β and M denote the wedge angle, the shock wave angle and the upstream Mach number, respectively. For the example under consideration with an inlet Mach number of 2.5, the exact value of the shock wave angle is of 36.94° at steady-state. From Fig. 7a, the numerical value of the shock wave angle can be measured and is found equal to 36.9° : the numerical and exact values are very close.

Table 11: Analytical solution for the supersonic flow on an edge eat 15° at $M = 2.5$.

	analytical downstream to upstream ratio	numerical downstream to upstream ratio
Pressure	2.47	2.467
Mach number	0.74	0.741
Entropy	1.03	1.026

The inlet is supersonic and therefore, the pressure, temperature and velocity are specified using Dirichlet boundary conditions. The outlet is also supersonic and none of the characteristics enter the domain through this boundary: the values will be computed by the implicit solver.

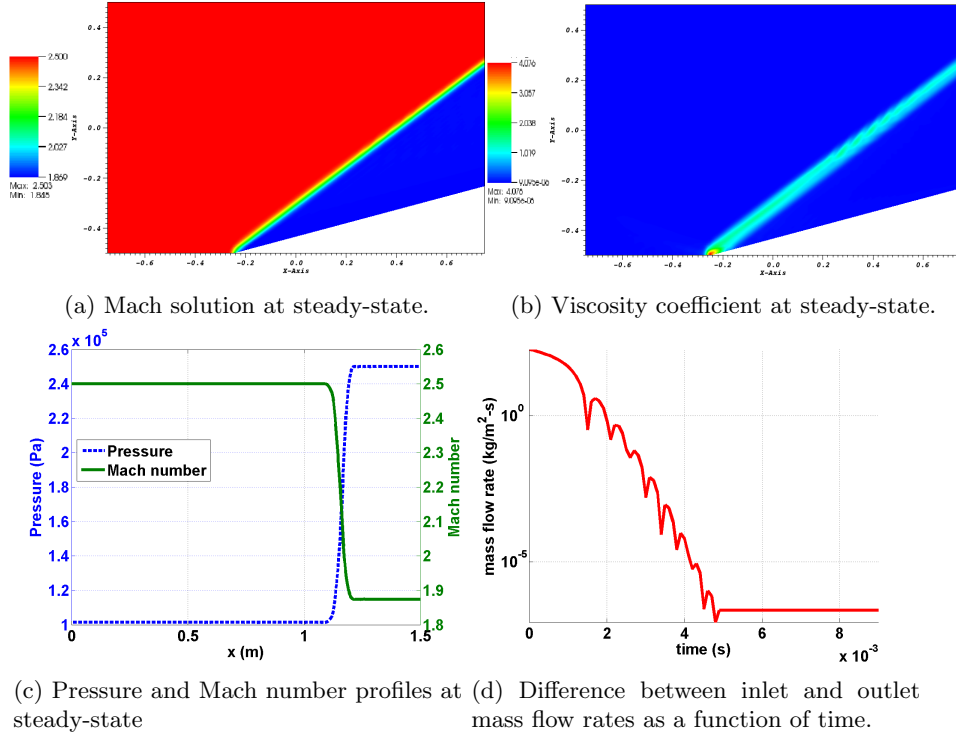


Figure 7: Steady-state solution for a flow in a 2-D compression corner.

685 The steady-state numerical solution is given in Fig. 7: the Mach number,
 686 the viscosity coefficients are plotted in Fig. 7a and Fig. 7b, respectively. The
 687 steady-state solution is formed of two regions of constant states, separated by
 688 the oblique shock. In Fig. 7b, the viscosity coefficient is large in the shock,
 689 small anywhere else, and thus, behaves as expected. At the corner of the edge
 690 at $x = -0.25$ m, the viscosity coefficient is peaked because of the treatment
 691 of the wall boundary condition: at this particular node, the normal is not well
 692 defined and can cause numerical errors. The 1-D plots of the pressure and the
 693 mach number at $y = 0$, are also given in Fig. 7c: the shock does not show any
 694 spurious oscillations and is well resolved. Finally, the difference between the
 695 inlet and outlet mass flow rates is plotted in Fig. 7d and show that the steady-
 696 state is reached.
 697 Overall, the numerical solution does not show any oscillations, match the ana-
 698 lytical solution, and the shock is well resolved.

699 6. Conclusions

700 A new version of the entropy viscosity method valid for a wide range of
 701 Mach number and applied to the multi-D Euler equations with variable area
 702 was derived and presented. The definition of the viscosity coefficient is now
 703 consistent with the low Mach asymptotic limit, does not require an analytical
 704 expression of the entropy function, and thus, could be used with any equation
 705 of state having a convex entropy. Tests were performed with the Ideal and
 706 Stiffened Gas equation of states. In 1-D, convergence of the numerical solu-
 707 tion (either smooth or with shocks) to the exact solution was demonstrated by
 708 computing the convergence rates of the L1 and L2 norms of the error for flows
 709 in convergence-divergent nozzle and a straight pipe. 2-D simulations were also
 710 performed for both subsonic and supersonic flows, and various geometries: the
 711 entropy viscosity method behaves well for a wide range of Mach number. The
 712 numerical results obtained for a flow over a circular bump (subsonic and tran-
 713 sonic flows) illustrates the capabilities of the method to adapt to the flow type.
 714 As future work, the entropy viscosity method will be extended to the 1-D seven
 715 equations model [19]. This two-phase flow system of equations is a good can-
 716 didate for two reasons: it is unconditionally hyperbolic and degenerates to the
 717 multi-D Euler equations when one phase disappears.

718 Acknowledgments

719 The authors would like to thank Bojan Popov and Jean-Luc Guermond for
 720 the many fruitful discussions.

721 References

- 722 [1] J. L. Guermond, R. Pasquetti, Entropy viscosity method for nonlinear con-
 723 servation laws, *Journal of Comput. Phys* 230 (2011) 4248–4267.

- [2] J. L. Guermond, R. Pasquetti, Entropy viscosity method for high-order approximations of conservation laws, *Lecture Notes in Computational Science and Engineering* 76 (2011) 411–418.
- [3] B. Cockburn, C. Johnson, C. Shu, E. Tadmor, Advanced numerical approximation of nonlinear hyperbolic equations, *Lecture Notes in Mathematics* 1697.
- [4] B. Cockburn, G. Karniadakis, C. Shu, Discontinuous galerkin methods: theory, computation and applications, *Lecture Notes in Computer Science and Engineering* 11.
- [5] R. Lohner, *Applied CFD Techniques: an Introduction based on Finite Element Methods*, 2nd Edition Wiley, 2003.
- [6] A. Lapidus, A detached shock calculation by second order finite differences, *J. Comput. Phys.* 2 (1967) 154–177.
- [7] R. Lohner, K. Morgan, J. Peraire, A simple extension to multidimensional problems of the artificial viscosity due to lapidus, *Commun. Numer. Methods Eng.* 1(14) (1985) 141–147.
- [8] J. Donea, A. Huerta, *Finite Element Methods for Flow Problems*, Oxford University Press, 2003.
- [9] H. Guillard, C. Viozat, On the behavior of upwind schemes in the low mach number limit, *Computers & Fluids* 28 (1999) 63–86.
- [10] E. Turkel, Preconditioned techniques in computational fluid dynamics, *Annu. Rev. Fluid Mech.* 31 (1999) 385–416.
- [11] J. S. W. D. L. Darmofal, J. Peraire, The solution of the compressible euler equations at low mach numbers using a stabilized finite element algorithm, *Comput. Methods Appl. Mech. Engrg.* 190 (2001) 5719–5737.
- [12] X.-S. Li, C.-W. Gu, An all-speed roe-type scheme and its asymptotic analysis of low mach number behavior, *Journal of Computational Physics* 227 (2008) 5144–5159.
- [13] J. L. Guermond, B. Popov, Viscous regularization of the euler equations and entropy principles, under review.
- [14] J. D. Anderson, Modern compressible flow, in: *Guide for Verification and Validation in Computational Solid Mechanic.*, New York, 1982, pp. 10–2006.
- [15] J. L. Guermond, R. Pasquetti, Entropy-based nonlinear viscosity for fourier approximations of conservation laws, in: *C.R. Math. Acad. Sci.*, Vol. 326, Paris, 2008, pp. 801–806.

- 760 [16] V. Zingan, J. L. Guermond, J. Morel, B. Popov, Implementation of the
761 entropy viscosity method with the discontinuous galerkin method, Journal
762 of Comput. Phys 253 (2013) 479–490.
- 763 [17] E. F. Toro, Riemann Solvers and numerical methods for fluid dynamics,
764 2nd Edition, Springer, 1999.
- 765 [18] B. Perthame, C. W. Shu, On positivity preserving finite volume schemes for
766 euler equations, Numer. Math. 73 (1996) 119–130.
- 767 [19] R. Berry, R. Saurel, O. LeMetayer, The discrete equation method (dem)
768 for fully compressible, two-phase flows in ducts of spatially varying cross-
769 section, Nuclear Engineering and Design 240 (2010) 3797–3818.
- 770 [20] B. Muller, Low-mach number asymptotes of the navier-stokes equations,
771 Journal of Engineering Mathematics 34 (1998) 97109.
- 772 [21] R. Loubere, Validation test case suite for compressible hydrodynamics com-
773 putation, Theoretical Division T-7 Los Alamos National Laboratory.
- 774 [22] D. L. Darmofal, K. Siu, A robust multigrid algorithm for the euler equations
775 with local preconditioning and semi-coarsening, Journal of Computational
776 Physics 151 (1999) 728756.
- 777 [23] P. Perrot, A to Z of Thermodynamics, Oxford University Press, 1998.
- 778 [24] O. LeMetayer, J. Massoni, R. Saurel, Elaborating equation of state for a
779 liquid and its vapor for two-phase flow models, International Journal of
780 Thermal Science 43 (2004) 265–276.
- 781 [25] S. LeMartelot, B. Nkonga, R. Saurel, Liquid and liquid-gas flows at all
782 speeds: Reference solutions and numerical schemes., Research report **why**
783 **not cite their jcp-2013?** 7935.
- 784 [26] R. A. DeVore, G. G. Lorentz, Constructive Approximation, Springer-
785 Verlag, 1991.
- 786 [27] H. Guillard, C. Viozat, On the behaviour of upwind schemes in the low
787 mach number limit, Comput. Fluids 105 (1993) 207–233.

788 **A. Derivation of the entropy residual as a function of the density, the**
 789 **pressure and the speed of sound:**

790 The entropy residual is often expressed as a function of the entropy $s(\vec{r}, t)$
 791 as follows:

$$D_e(\vec{r}, t) = \partial_t s(\vec{r}, t) + \vec{u} \cdot \vec{\nabla} \cdot s(\vec{r}, t)$$

792 where all variables were defined previously. This form of the entropy residual is
 793 not suitable for the low-Mach limit as explained in Section 2.1. It can be shown
 794 that the entropy residual $D_e(\vec{r}, t)$ can be recast as a function of the primitive
 795 variables (pressure, velocity and density) and the speed of sound. This is the
 796 objective of this appendix.

797 The first step is to use the chain rule, remembering that the entropy is assumed
 798 function of the internal energy e and the density ρ :

$$D_e(\vec{r}, t) = s_e \frac{de}{dt} + s_\rho \frac{d\rho}{dt}$$

799 where s_x denotes the partial derivative of s with respect to the variable x . The
 800 short-notation $\frac{d}{dt}$ is used for the total or material derivative. We no need to
 801 make the pressure appear: this can be achieved by noticing that the internal
 802 energy is a function of the pressure and the density based on the definition of
 803 the equation of state. Once again, by using the chain rule, it yields:

$$\begin{aligned} D_e(\vec{r}, t) &= s_e e_P \frac{dP}{dt} + (s_e e_\rho + s_\rho) \frac{d\rho}{dt} \\ &= s_e e_P \left(\frac{dP}{dt} + \frac{1}{s_e e_P} (s_e e_\rho + s_\rho) \frac{d\rho}{dt} \right) \\ &= s_e e_P \left(\frac{dP}{dt} + \left(\frac{e_\rho}{e_P} + \frac{s_\rho}{s_e e_P} \right) \frac{d\rho}{dt} \right) \end{aligned}$$

804 We are now close to the final result (see Eq. (8)). It remains to prove that the
 805 term multiplying the material derivative of the density is equal to the speed
 806 of sound square. The speed of sound is often defined as the partial derivative
 807 of the pressure with respect to the density at constant entropy, which can be
 808 recast as a function of the entropy as follows (see Appendix A.2 of [13]):

$$c^2 = \left(\frac{\partial P}{\partial \rho} \right)_s = P_\rho - \frac{s_\rho}{s_e} P_e = -\frac{e_\rho}{e_P} - \frac{s_\rho}{s_e e_P}$$

809 using the following relations (see Appendix A.1 of [13]):

$$P_e = \frac{1}{e_P} \text{ and } P_\rho = -\frac{e_\rho}{e_P}$$

810 Then, the result follows.

811 **B. Derivation of the dissipative terms for the multi-D Euler equations**
 812 **with variable area using the entropy minimum principle:**

813 The multi-D Euler equations with variable area are recalled here:

$$\begin{cases} \partial_t (\rho A) + \vec{\nabla} \cdot (\rho \vec{u} A) = 0 \\ \partial_t (\rho \vec{u} A) + \vec{\nabla} \cdot [A (\rho \vec{u} \otimes \vec{u} + P \mathbf{I})] = P \vec{\nabla} A \\ \partial_t (\rho E) + \vec{\nabla} \cdot [\vec{u} (\rho E + P)] = 0 \end{cases}$$

814 Assuming the existence of an entropy s function of the density ρ and the internal
 815 energy e , the above system of equations admits the following entropy residual
 816 [17]:

$$A \rho \left(\partial_t s + \vec{u} \cdot \vec{\nabla} \cdot s \right) \geq 0$$

817 when assuming $P s_e + \rho^2 s_\rho = 0$. An entropy function s verifying this equation
 818 is also a solution of the second thermodynamic law for a reversible system,
 819 $T ds = de - \frac{P}{\rho^2} d\rho$, which implies $s_e = T^{-1} \geq 0$.

820 In order to apply the entropy viscosity method, dissipative terms are added to
 821 each equation. Then, the entropy residual is derived again: extra terms due to
 822 the dissipative terms will appear in the left-hand side. In order to prove the
 823 minimum entropy principle, these extra terms are either recast as conservative
 824 term, or shown to be positive.

825 The multi-D Euler equations with variable area with dissipative terms, yield:

$$\begin{cases} \partial_t (\rho A) + \vec{\nabla} \cdot (\rho \vec{u} A) = \vec{\nabla} \cdot f \\ \partial_t (\rho \vec{u} A) + \vec{\nabla} \cdot [A (\rho \vec{u} \otimes \vec{u} + P \mathbf{I})] = P \vec{\nabla} A + \vec{\nabla} \cdot g \\ \partial_t (\rho E) + \vec{\nabla} \cdot [\vec{u} (\rho E + P)] = \vec{\nabla} \cdot h \end{cases} \quad (32)$$

826 where f , g and h are the dissipative terms to derive. Starting from the modified
 827 system of equations given in Eq. (32), the entropy residual is derived again:

$$\begin{aligned} A \rho \left(\partial_t s + \vec{u} \cdot \vec{\nabla} \cdot s \right) &= s_e \left[\vec{\nabla} \cdot h + g \vec{\nabla} u + \left(\frac{u^2}{2} - e \right) \vec{\nabla} \cdot f \right] \\ &+ \rho s_\rho \vec{\nabla} \cdot f \end{aligned} \quad (33)$$

828 The next step consists of choosing a definition for each of the dissipative terms
 829 so that the left hand-side is proven positive. The right hand-side of Eq. (33)
 830 can be simplified using the following relations, $g = A \mu \vec{\nabla}^s \vec{u} + \vec{u} \otimes f$ and $h =$
 831 $\tilde{h} + \vec{u} \cdot g - 0.5 ||\vec{u}||^2 f$, which yields:

$$A \rho \left(\partial_t s + \vec{u} \cdot \vec{\nabla} \cdot s \right) = s_e \left[\vec{\nabla} \cdot \tilde{h} - e \vec{\nabla} \cdot f \right] + \rho s_\rho \vec{\nabla} \cdot f + A s_e \mu \vec{\nabla}^s \vec{u} \cdot \vec{\nabla} \vec{u}$$

832 The right hand-side is now integrated by parts:

$$\begin{aligned} A \rho \left(\partial_t s + \vec{u} \cdot \vec{\nabla} \cdot s \right) &= \vec{\nabla} \cdot \left[s_e \tilde{h} - s_e e f + \rho s_\rho f \right] - \\ &\vec{\nabla} \cdot \tilde{h} \vec{\nabla} s_e - f \vec{\nabla} (e s_e) - f \vec{\nabla} (\rho s_\rho) + A s_e \mu \vec{\nabla}^s \vec{u} \cdot \vec{\nabla} \vec{u} \end{aligned}$$

833 where $\vec{\nabla}^s$ is the symmetric gradient. The term $As_e\mu\vec{\nabla}\vec{u}^s\vec{\nabla}\vec{u}$ is positive and thus,
 834 does not need any further modification. It remains to treat the other terms of
 835 the right hand-side that we now call rhs :

$$rhs = \vec{\nabla} \cdot [s_e \tilde{h} - s_e e f + \rho s_\rho f] - \cancel{\tilde{h}} \vec{\nabla} s_e - f \vec{\nabla} (e s_e) - f \vec{\nabla} (\rho s_\rho)$$

836 The first term of rhs is a conservative terms. By choosing carefully a definition
 837 for \tilde{h} and f , the conservative term can be expressed as a function of the entropy
 838 s . It is also required to include the variable area in the choice of the dissipative
 839 terms so that when assuming constant area, the regular multi-D Euler equations
 840 are recovered. The following definitions for \tilde{h} and f are chosen:

$$\tilde{h} = A\kappa\vec{\nabla}(\rho e) \text{ and } f = A\kappa\vec{\nabla}\rho,$$

841 which yields, using the chain rule:

$$rhs = \vec{\nabla} \cdot (\rho A\kappa\vec{\nabla}s) - A\kappa \underbrace{\left[\vec{\nabla}(\rho e)\vec{\nabla}s_e + \vec{\nabla}\rho\vec{\nabla}(e s_e) + \vec{\nabla}\rho\vec{\nabla}(\rho s_\rho) \right]}_{\mathbf{Q}}$$

842 It remains to treat the term \mathbf{Q} that can be recast under a quadratic form,
 843 following the work done in [13]:

$$\begin{aligned} \mathbf{Q} &= X^t \Sigma X \\ \text{with } X &= \begin{bmatrix} \vec{\nabla}\rho \\ \vec{\nabla}e \end{bmatrix} \text{ and } \Sigma = \begin{bmatrix} \partial_\rho(\rho^2 \partial_\rho s) & \partial_{\rho,e}s \\ \partial_{\rho,e}s & \partial_{e,e}s \end{bmatrix} \end{aligned}$$

844 The matrix Σ is symmetric and identical to the matrix obtained in [13]. The sign
 845 of the quadratic form can be simply determined by studying the positiveness of
 846 the matrix Σ . In this particular case, it is required to prove that the matrix is
 847 negative definite: the quadratic form is in the right hand-side and is preceded of
 848 a negative sign. According to [13], the convexity of the opposite of the entropy
 849 function s with respect to the internal energy e and the specific volume $1/\rho$ is
 850 sufficient to ensure that the matrix Σ is negative definite.

851 Thus, the right hand-side of the entropy residual Eq. (33), are now either recast
 852 as conservative terms, or known to be positive. Following the work done by [13],
 853 the entropy minimum principle holds.